Materials Transactions, Vol. 64, No. 10 (2023) pp. 2410 to 2416
Special Issue on Metallurgy for Advanced Catalytic Materials

Metallic Honeycomb Catalysts for Methane Steam Reforming: Effect of the Bimetallic Surface Coating on Catalytic Properties

Tsukasa Nakasone[1,2,*1], Ya Xu[2,*2] and Ryuji Tamura[1]

[1]*Department of Materials Science and Technology, Tokyo University of Science, Tokyo 125-8585, Japan*
[2]*Center for Green Research on Energy and Environmental Materials, National Institute for Materials Science, Tsukuba 305-0003, Japan*

Metallic honeycomb catalysts are promising candidates for fuel cell and small-scale onsite hydrogen production applications. In this study, high-cell-density Ni honeycomb catalysts coated with a series of bimetallic surface layers were synthesized. Their catalytic performance for CH_4 steam reforming was investigated under a low steam-to-carbon ratio of 1.36 and a gas hourly space velocity of 6400 h^{-1} in the temperature range of 400–700°C. The catalysts coated with Ni–Mg and Ni–Zr showed excellent catalytic performance, reaching a high CH_4 conversion and CO selectivity close to the equilibrium values within the test temperature range. The enhanced catalytic performance of the Ni–Mg and Ni–Zr coatings was attributed to the formation of oxide-supported fine Ni particles. In contrast, the catalysts coated with Ni–Fe and Ni–Sn exhibited an extremely low activity, which was lower than that of the catalyst coated with only Ni. The low activity of the Ni–Fe and Ni–Sn coatings is supposed to be due to the formation of aggregated Ni_3Fe, Ni_3Sn, and Ni_3Sn_2 phases. [doi:10.2320/matertrans.MT-MH2022005]

(Received April 3, 2023; Accepted April 24, 2023; Published May 19, 2023)

Keywords: *metallic honeycomb catalyst, nickel-based bimetallic coating, methane steam reforming, hydrogen production*

1. Introduction

It is essential to develop efficient, low-cost, and small-scale hydrogen production systems for fuel cell and small-scale onsite hydrogen production applications.[1–3] High-performance and low-cost catalysts are required for hydrogen production systems. Metallic honeycomb catalysts are more promising than conventional pellet-type catalysts because they have several advantages, such as a low pressure drop per catalyst volume, compactness, and high heat and mass transfer abilities.[4–9]

In recent years, metallic honeycomb catalysts have been studied for hydrogen production reactions. Fukuhara *et al.* fabricated a structured Ni/Al_2O_3 catalyst by combining a sol-gel method to form an Al_2O_3 layer and electroless plating to deposit a Ni component on a stainless-steel honeycomb fin. The prepared catalyst exhibited a high activity in CH_4 steam reforming (MSR).[10,11] We also developed a metallic honeycomb catalyst using pure Ni thin foil with a high cell density of 900 cpsi (number of cells per square inch) for MSR.[12] The prepared catalyst exhibited a high activity and an excellent carbon deposition resistance for MSR at 800°C for over 8000 h at a low steam-to-carbon ratio (S/C = 1.34) and gas hourly space velocity (GHSV = 335 h^{-1}). The activity of this honeycomb catalyst was further improved by increasing the cell density of the honeycomb to 2300 cpsi and performing steam pretreatment prior to the reaction.[13,14] Furthermore, to enhance the catalytic performance of the Ni honeycomb catalyst for MSR at low temperatures (<800°C), a Ni–Re bimetallic layer was synthesized directly on the surfaces of Ni honeycomb channels without the use of an oxide support, which maintains the high thermal conductivity of the honeycomb.[15] The activity of the honeycomb catalyst below 700°C was effectively improved by the formation of Ni–Re bimetallic surface layer, which indicates that the catalytic activity of metallic honeycombs can be improved by controlling the composition and microstructure of the surface coating layer. In addition, intermetallic compounds are known to exhibit different catalytic properties from those of component pure metals;[16,17] for example, Ni_3Al and $Ni_3(Si,Ti)$ in the form of foils[18,19] and Ni_3Fe and Ni_3Sn in the form of nanoparticles[20,21] both showed high activity for methanol decomposition. The aim of this study was to synthesize various Ni–X (X = Zr, Mg, Sn, or Fe) bimetallic or intermetallic surface layers on Ni metallic honeycomb substrates and to examine their catalytic activity for MSR to develop low-cost, high-performance metallic honeycomb catalysts.

2. Experimental Procedure

2.1 Catalyst preparation

The Ni honeycomb substrate with a cell density of 2300 cpsi was fabricated using flat and corrugated thin Ni foils with a thickness of 30 μm. The flat Ni foils were fabricated by forging, hot-rolling, and cold-rolling commercially available pure Ni ingots. The corrugated files were shaped in an approximate sinusoidal waveform (height of 0.4 mm and spacing of 1 mm). The honeycomb substrate was cylindrical, with a diameter and height of 8 and 10 mm, respectively (Fig. 1), and it weighed approximately 0.6 g. The fabricated honeycomb was degreased with acetone, activated with diluted nitric acid (10 vol% HNO_3 aqueous solution), and coated with a surface layer using a method similar to the conventional sequential impregnation method for preparing supported catalysts with two sequential solutions, A and B. Solution A was a $Ni(NO_3)_2{\cdot}6H_2O$ (FUJIFILM Wako Pure Chem. Co.) aqueous solution that consisted of 5 mass% Ni relative to the weight of the honeycomb substrate. Solution B was an aqueous solution consisting of one of the following: $ZrO(NO_3)_2{\cdot}2H_2O$, $Mg(NO_3)_2{\cdot}6H_2O$, $Fe(NO_3)_2{\cdot}9H_2O$, or $SnCl_2{\cdot}2H_2O$ (FUJIFILM Wako Pure Chem. Co.), each of which contained a third (molar ratio) of the amount of Ni

*1Graduate Student, Tokyo University of Science. Present address: Niihama Nickel Refinery, Sumitomo Metal Mining Co. Ltd., Niihama 792-8555, Japan
*2Corresponding author, E-mail: XU.Ya@nims.go.jp

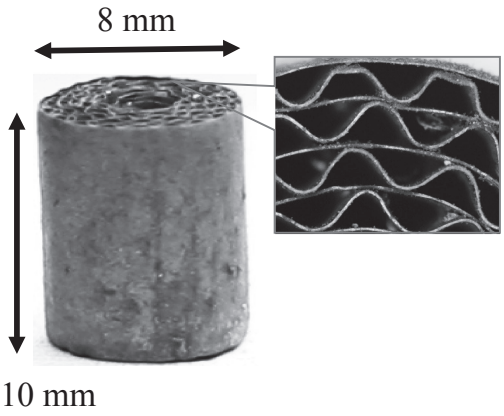

Fig. 1 The fabricated Ni honeycomb structure with a cell density of 2300 cpsi.

in solution A as a second element, thereby obtaining surface layer compositions (by molar ratio) of Ni_3Mg, Ni_3Zr, Ni_3Fe, or Ni_3Sn, respectively. The surface layer was formed by impregnating the honeycomb with solution A and drying at 120°C for 12 h, followed by impregnation with solution B, drying in the same manner, and calcination at 500°C for 4 h in air. Hereafter, the prepared samples are denoted as Ni–Zr, Ni–Mg, Ni–Fe, and Ni–Sn, and the sample without a second element (impregnated with solution A only) is denoted as Ni–0.

2.2 Catalytic reaction test

MSR tests were conducted on the fabricated Ni honeycomb samples using a fixed-bed reactor at ambient pressure. Prior to the catalytic reaction test, a hydrogen reduction treatment was performed at 430°C for 1 h in a flow gas mixture of H_2 and N_2 at flow rates of 30 and 5 mL min^{-1}, respectively. All reported gas volumes in this study correspond to the values at a standard temperature and pressure (STP, 0°C, 1 atm). After the hydrogen reduction, H_2 was purged by an N_2 flow gas. Catalytic reaction tests were conducted at gas flow rates of 10, 13.6, and 30 mL min^{-1} for CH_4, H_2O (steam), and N_2, respectively, and with an S/C of 1.36 and GHSV of 6400 h^{-1}. Two types of catalytic reaction tests were conducted, namely a stepwise heating test from 400–700°C that was increased in 100°C increments, which were each maintained for 5 h, and an isothermal test at 700°C for 20 h. Data was collected using two on-line gas chromatographs (GC; GL Science, GC323). One was equipped with a column packed with zeolite (Molecular Sieve 13X) to detect H_2, N_2, CH_4, and CO, whereas the other was equipped with a column packed with a porous polymer sorbent (Porapak Q) to detect CO_2 and H_2O. The flow rate of each component during the reaction was determined based on the flow rate of the N_2 gas and the composition of the output gases analyzed by the GCs. The CH_4 conversion (X_{CH4}), hydrogen yield ($STY\text{-}H_2$), CO selectivity (S_{CO}), and CO_2 selectivity (S_{CO2}) were calculated using eqs. (1)–(4):

$$X_{CH_4} = F_{CH_4}/F^0_{CH_4} \times 100 \quad (1)$$

$$STY - H_2 = F_{H_2}/A \quad (2)$$

$$S_{CO} = F_{CO}/(F_{CO} + F_{CO_2}) \times 100 \quad (3)$$

$$S_{CO_2} = F_{CO_2}/(F_{CO} + F_{CO_2}) \times 100 \quad (4)$$

where $F^0{}_{CH4}$ is the flow rate of the supplied CH_4 (mol s^{-1}), and F_{CH4}, F_{H2}, F_{CO}, and F_{CO2} are the outlet flow rates (mol s^{-1}) of CH_4, H_2, CO, and CO_2, respectively. The hydrogen yield (eq. (2)) is defined as the H_2 flow rate per unit time (mol m^{-2} s^{-1}) and is normalized by the geometric surface area of the honeycomb substrate A (m^2).

2.3 Characterization

X-ray diffraction (XRD) measurements were performed to identify the phase of the coating layer after the calcination and hydrogen reduction treatment (Rigaku; MiniFlex 600, Cu Kα line, 40 kV, 15 mA). A temperature-programmed reduction (TPR) measurement was performed to determine the reduction temperature at a heating rate of 10°C min^{-1} from 25 to 1000°C in a stream (50 mL min^{-1}) of H_2 diluted with Ar (4 vol% H_2).

The surface morphologies of the samples were observed using scanning electron microscopy (SEM; JEOL; JSM-7000F, acceleration voltage: 20 kV). The Brunauer–Emmett–Teller (BET) specific surface area of each sample was measured via N_2 adsorption using a specific-surface-area-measuring device (Micromeritics, ASAP2020).

Transmission electron microscopy (TEM) and scanning transmission electron microscopy (STEM) were performed using a field-emission transmission electron microscope equipped with an energy-dispersive spectrometry (EDS) analysis system (JEOL, JEM-2100F) at an acceleration voltage of 200 kV. EDS elemental mapping was performed in the STEM mode.

3. Results and Discussions

3.1 Catalyst properties

Figure 2 shows the CH_4 conversion of the honeycomb catalysts coated with Ni–Mg, Ni–Zr, Ni–Fe, Ni–Sn, and Ni–0 during the stepwise heating test. For comparison, the results

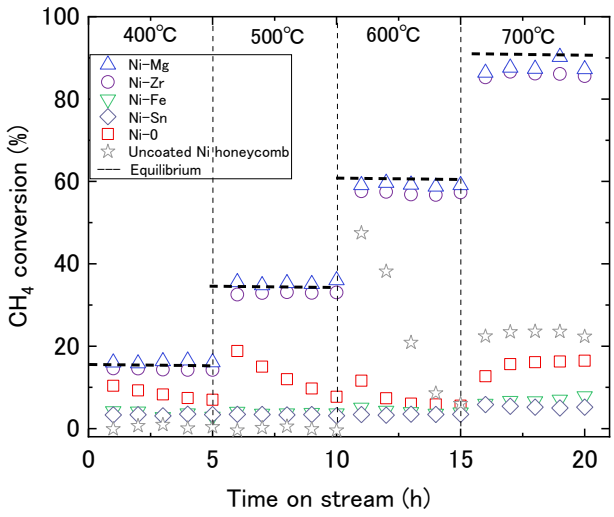

Fig. 2 The CH_4 steam reforming catalytic performance of the Ni honeycomb catalysts coated with various bimetallic surface layers during the stepwise heating test. For comparison, the results of the uncoated Ni honeycomb substrate are also shown.

of the Ni honeycomb substrate without coating are also shown in Fig. 2. The catalysts coated with Ni–Mg and Ni–Zr showed much higher CH_4 conversions that were very close to the equilibrium values at all test temperatures, whereas those coated with Ni–Fe and Ni–Sn showed much lower CH_4 conversions at all test temperatures. The CH_4 conversion of the sample coated with only Ni (Ni–0) was slightly higher than those of Ni–Fe and Ni–Sn but much lower than those of Ni–Mg and Ni–Zr. In addition, in contrast to the relatively stable CH_4 conversion values of the Ni–Mg, Ni–Zr, Ni–Fe, and Ni–Sn samples during the keeping period (5 h) at each temperature, the CH_4 conversion of the Ni–0 sample gradually decreased with an increase in the keeping time at temperatures below 600°C (Fig. 2). This is likely due to the aggregation of Ni particles easily occurred in the Ni–0 sample. The Ni honeycomb substrate without coating showed no activity below 500°C; at 600°C, however, it exhibited a relatively high initial CH_4 conversion, but this activity decreased quickly with the increasing holding time. Furthermore, at 700°C, it showed a slightly higher CH_4 conversion than the Ni-coated sample (Ni–0). These results indicate that the bare Ni honeycomb can exhibit relatively high activity at high temperatures, which is agreement with our previous results.[13)]

Figure 3 shows the CH_4 conversion of the honeycomb catalysts as a function of time on the stream during the isothermal tests at 700°C. The Ni–Mg and Ni–Zr samples exhibited an initial CH_4 conversion of approximately 90%, which was close to the equilibrium conversion of 92%. The conversion value did not significantly decrease during the whole period (20 h) at 700°C. In contrast, the Ni–Fe, Ni–Sn, and Ni–0 samples exhibited much lower initial CH_4 conversions. Ni–Fe initially showed a CH_4 conversion of 25%, which gradually decreased over time and stabilized at 7% after 6 h. Ni–Sn retained its initial CH_4 conversion of 7% throughout the test. The Ni–0 sample showed an initial CH_4 conversion of 13%, which slightly increased over time, reaching approximately 20% after 20 h. On the other hand, the Ni honeycomb substrate without coating showed a restively stable CH_4 conversion around 30% throughout the test at 700°C, which agreed with our previous report, and was higher than those of Ni–0, Ni–Fe, and Ni–Sn samples.

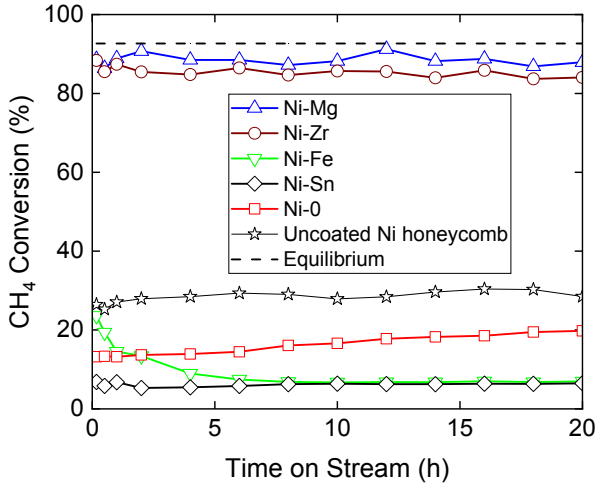

Fig. 3 The CH_4 conversion of the Ni honeycomb catalysts coated with various bimetallic surface layers during the isothermal test at 700°C. For comparison, the results of the uncoated Ni honeycomb substrate are also shown.

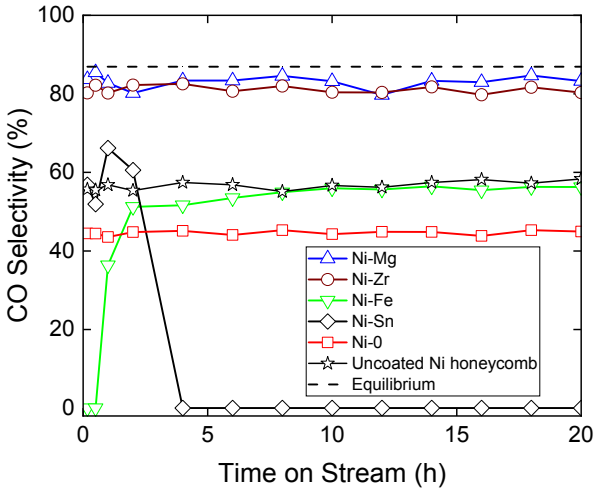

Fig. 4 The CO selectivity of the Ni honeycomb catalysts coated with various bimetallic surface layers and the uncoated Ni honeycomb substrate during the isothermal test at 700°C.

The CO selectivity in the isothermal test is shown as a function of time on the stream in Fig. 4. The Ni–Mg and Ni–Zr samples exhibited high and stable CO selectivity above 80%, which was close to the equilibrium value of 87% during the test. This indicated that the Ni–Mg and Ni–Zr samples had a high selectivity for MSR. In contrast, the Ni–Fe, Ni–Sn, and Ni–0 samples exhibited much lower CO selectivity than Ni–Mg and Ni–Zr. The Ni–Fe sample showed an initial CO selectivity of 0%, which rapidly increased to approximately 50%, whereas the Ni–Sn sample showed exhibited an initial CO selectivity of approximately 60% before rapidly decreasing to 0% after 4 h. The Ni–0 sample exhibited a CO selectivity of approximately 45%, which remained nearly unchanged during the test. By contrast, the uncoated Ni honeycomb substrate showed a CO selectivity of approximately 55%, which was slightly higher than that of the Ni–0 sample. These results indicate that the Ni–Mg and Ni–Zr catalysts have a high activity, stability, and selectivity for MSR. In contrast, the Ni–Fe and Ni–Sn samples exhibited a low activity and selectivity for MSR.

3.2 Characterization

3.2.1 X-ray diffraction and temperature-programmed reduction results

Figure 5 shows the XRD profiles of the Ni–Mg, Ni–Zr, Ni–Fe, Ni–Sn, and Ni–0 surface layers in their calcination states (Fig. 5(a)) and after hydrogen reduction at 430°C for 1 h (Fig. 5(b)). For the calcined samples, all the diffraction peaks were identified as oxide phases: ($MgNiO_2 + NiO$) in the Ni–Mg sample, ($ZrO_2 + NiO$) in the Ni–Zr sample, ($Fe_3O_4 + NiO$) in the Ni–Fe sample, ($SnO_2 + NiO$) in the Ni–Sn sample, and NiO in the Ni–0 sample. After hydrogen reduction, peaks from the metallic Ni phase were identified, whereas peaks from $MgNiO_2$ and ZrO_2 were retained in the Ni–Mg and Ni–Zr samples, indicating that only NiO was reduced to metallic Ni. $MgNiO_2$ and ZrO_2 were not reduced by the reduction treatment. In contrast, peaks from the Ni_3Fe

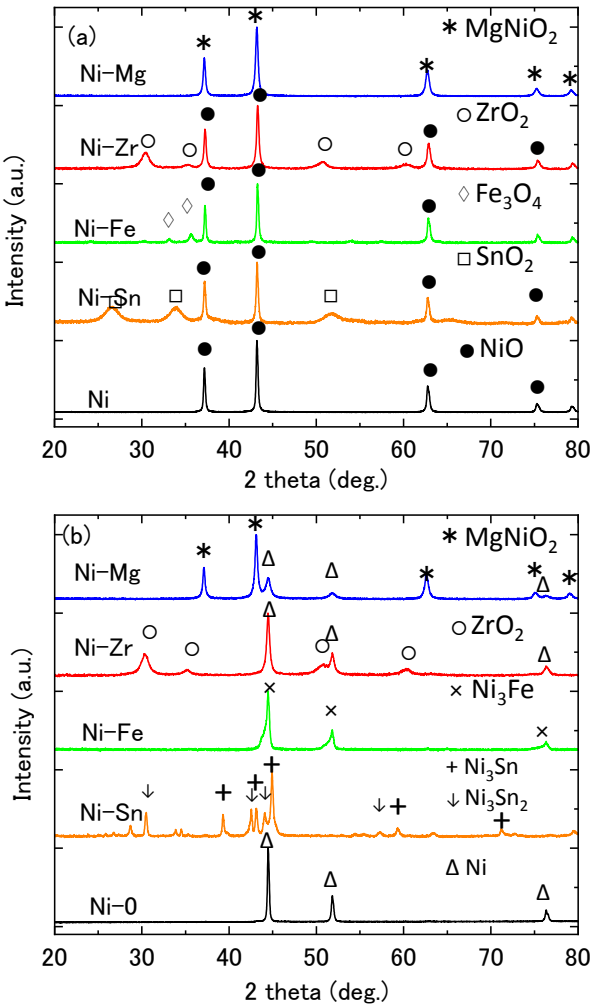

Fig. 5 X-ray diffraction profiles of the Ni–Mg, Ni–Zr, Ni–Fe, Ni–Sn, and Ni–0 surface layers after (a) calcination at 500°C for 4 h in air and (b) H_2 reduction at 430°C for 1 h in a mixture of H_2 and N_2 at flow rates of 30 and 5 mL min^{-1}, respectively.

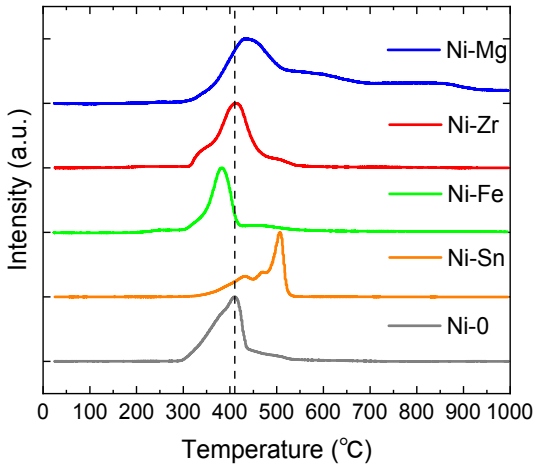

Fig. 6 Temperature-programmed reduction profiles of the Ni–Mg, Ni–Zr, Ni–Fe, Ni–Sn, and Ni–0 surface layers after calcination at 500°C for 4 h. The measurements were performed from room temperature to 1000°C at a heating rate of 10°C min^{-1} and an H_2/Ar flow (4 vol% H_2) of 50 mL min^{-1}.

Table 1 Brunauer–Emmett–Teller specific surface areas ($m^2\ g^{-1}$) of honeycomb catalysts coated with various bimetallic surface layers.

Sample	After reduction	After stepwise heating test	After isothermal test at 700℃
Ni-Mg	2.24	1.11	0.83
Ni-Zr	1.12	0.57	0.34
Ni-Fe	0.57	0.21	0.21
Ni-Sn	0.32	0.23	0.18
Ni-0	0.38	0.19	0.11

phase were identified in the Ni–Fe sample, and no peaks from the Fe and Ni oxides were observed, suggesting that both NiO and Fe_3O_4 were reduced to metallic Ni and Fe and further combined to form Ni_3Fe during the hydrogen reduction treatment. Peaks from the Ni_3Sn and Ni_3Sn_2 phases were identified in the Ni–Sn sample, together with some weak peaks from SnO_2. This suggests that NiO and part of SnO_2 were reduced to metallic Ni and Sn and that they were combined further to form the Ni_3Sn and Ni_3Sn_2 phases. In addition, only metallic Ni phase was identified in the Ni–0 sample, indicating that NiO was completely reduced to metallic Ni by the hydrogen reduction treatment at 430°C.

Figure 6 shows the TPR profiles of the samples in their calcined states. A reduction peak at approximately 410°C was detected in Ni–0 sample, which is supposed to correspond to the reduction of NiO.[22] A main reduction at approximately 510°C and two broad peaks at approximately 420°C and 460°C were observed in the Ni–Sn sample. The peak at approximately 510°C is supposed to correspond to the reduction of SnO_2[23,24] and the broad peaks correspond to reduced NiO and SnO_2.[22–24] A reduction peak at approximately 385°C was detected in the Ni–Fe sample, which is supposed to correspond to the reduction of Fe_3O_4 and NiO. Noting that the temperature was slightly lower than that of the Ni–0 sample, the combination of Ni and Fe oxides may be reduced more easily than that of Ni oxide. A main reduction at 410–450°C was observed in both Ni–Mg and Ni–Zr, which is supposed to correspond to the reduction of NiO. These TPR results are consistent with the XRD results, suggesting that NiO, Fe_3O_4, and a part of SnO_2 were reduced by the reduction treatment at 430°C.

3.2.2 Brunauer–Emmett–Teller specific surface area

Table 1 shows the BET specific surface areas of the samples after they underwent reduction treatment, a stepwise heating test, and an isothermal test at 700°C. For the samples after the hydrogen reduction, the BET specific surface areas of Ni–Mg and Ni–Zr were 2.24 and 1.12 $m^2\ g^{-1}$, respectively, which were significantly larger than those of Ni–Fe, Ni–Sn, and Ni–0 (0.57, 0.32, and 0.38 $m^2\ g^{-1}$, respectively). After the stepwise heating and isothermal tests, the BET specific surface areas of all samples significantly decreased. However, the BET specific surface areas of the Ni–Mg and Ni–Zr samples remained larger than those of the other samples.

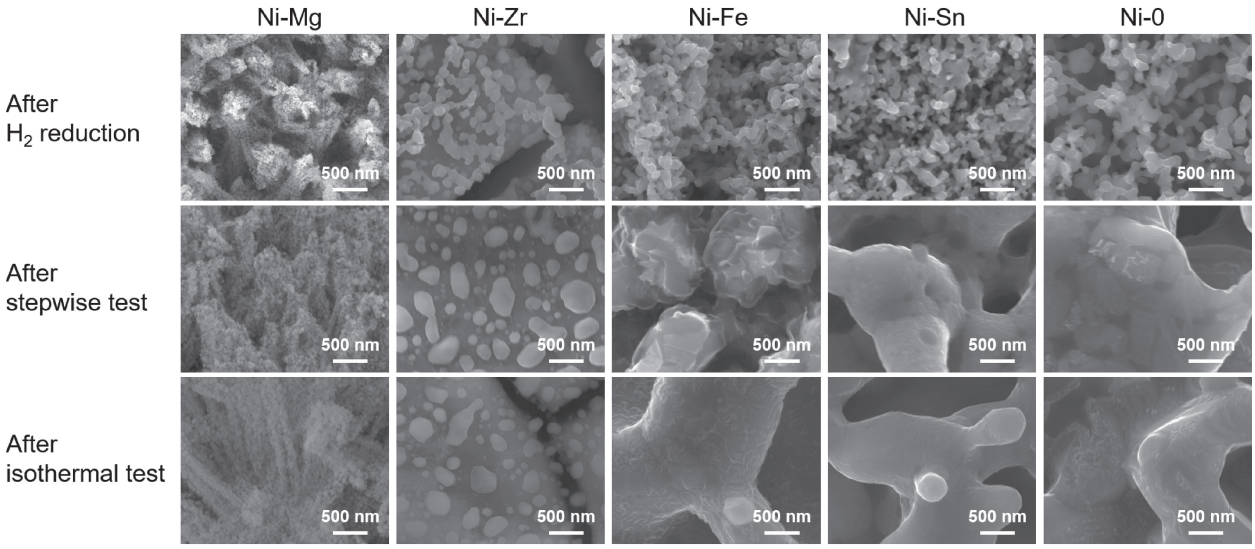

Fig. 7 Scanning electron microscopy secondary electron images of the surface of the Ni honeycomb catalysts coated with Ni–Mg, Ni–Zr, Ni–Fe, Ni–Sn, and Ni–0 after hydrogen reduction at 430°C for 1 h (upper), a stepwise heating test from 400–700°C (middle), and an isothermal test at 700°C for 20 h (lower).

3.2.3 Scanning and transmission electron microscopy analyses

The surface microstructures of the samples after hydrogen reduction, stepwise testing, and isothermal testing were observed using SEM (Fig. 7). In the reduced samples, a large number of extremely fine particles with sizes less than a few dozen nanometers were observed in the Ni–Mg sample. In contrast, fine particles with sizes ranging from several dozens to several hundreds of nanometers were observed in the other samples, that is, Ni–Zr, Ni–Fe, Ni–Sn, and Ni–0. In the case of Ni–Zr, fine particles were observed to be supported on some lumps. Significant particle agglomeration was observed in Ni–Fe, Ni–Sn, and Ni–0 after the stepwise and isothermal tests. In contrast, the agglomeration of particles was relatively minor in Ni–Zr and Ni–Mg after both the stepwise and isothermal tests.

Figure 8 shows the TEM image (Fig. 8(a)) and STEM-EDS element mapping (Fig. 8(b)) of the Ni–Mg surface layer after hydrogen reduction. Fine Ni particles with a size of a few dozen nanometers or less were confirmed to be distributed homogeneously with Mg and O. This is likely due to the Ni and $NiMgO_2$ phases mixing, as identified by the XRD measurements (Fig. 5).

Figure 9 shows the TEM image (Fig. 9(a)) and STEM-EDS element mapping (Fig. 9(b)) of the Ni–Zr surface layer after hydrogen reduction. Fine Ni particles that had diameters of 100–200 nm were distributed in a clump consisting of Zr and O. This clump was assumed to be the ZrO_2 phase, considering the XRD measurement results (Fig. 5).

3.3 Effect of surface coating on catalytic performance

These results revealed that the surface coating composition significantly affected the MSR catalytic performance of the metallic honeycomb catalyst. The Ni–Mg and Ni–Zr coatings significantly improved the catalytic activity and selectivity for MSR, whereas the Ni–Fe and Ni–Sn coatings decreased the MSR selectivity with the Ni–0 coating (Figs. 2–4). The high catalytic activity of Ni–Zr and Ni–Mg is attributed to the microstructure generated during the hydrogen reduction treatment, that is, fine Ni particles supported on the metal oxides $NiMgO_2$ or ZrO_2, which showed less aggregation of

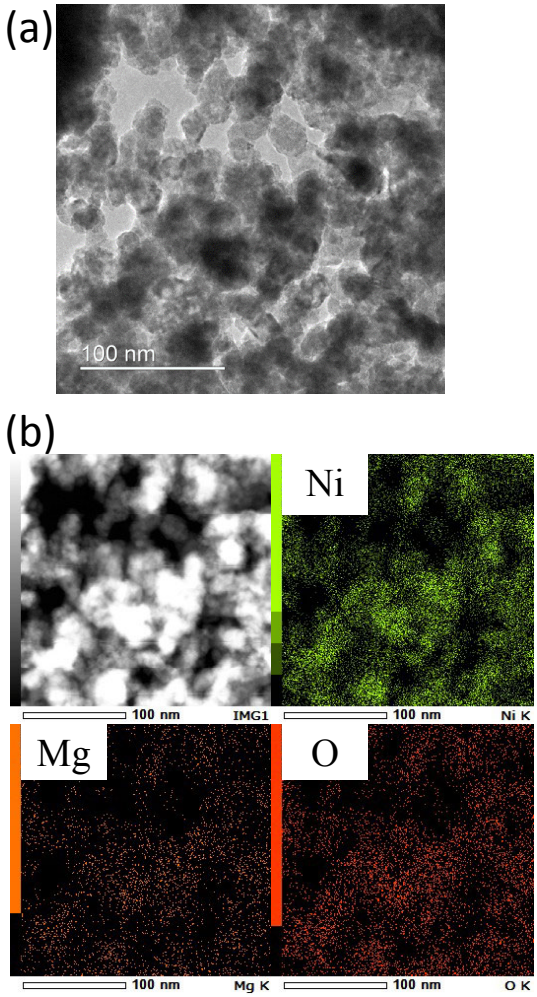

Fig. 8 (a) A transmission electron microscopy (TEM) image and (b) annular dark-field (ADF)-STEM and elemental mapping images of the Ni–Mg surface layer after hydrogen reduction.

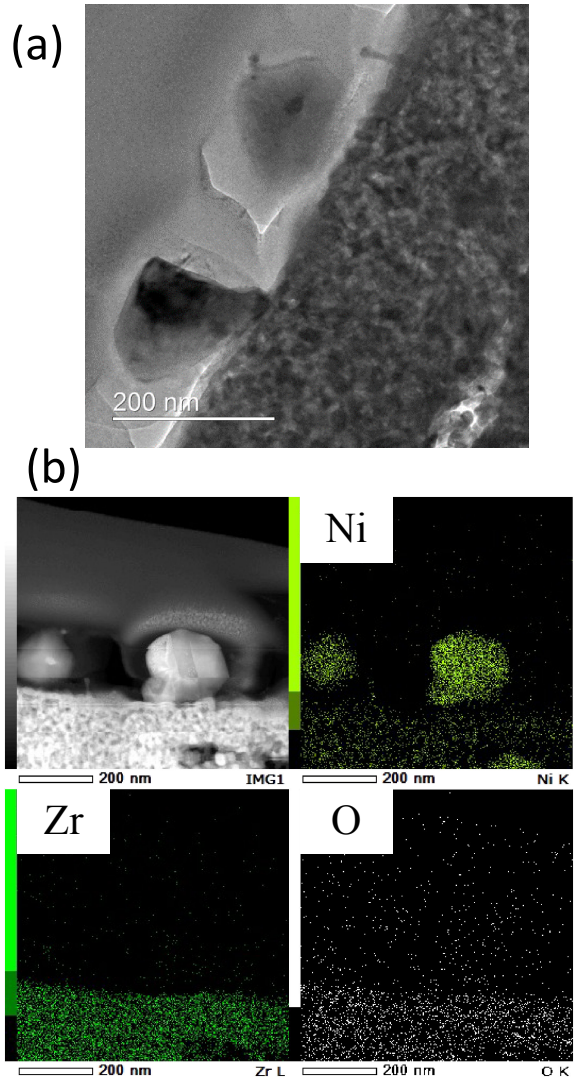

Fig. 9 (a) A TEM image and (b) ADF-STEM and elemental mapping images of the Ni–Zr surface layer after hydrogen reduction.

fine Ni particles during the reaction (Figs. 7–9) and retained a relatively large BET specific surface area (Table 1). The $NiMgO_2$ and ZrO_2 formed during calcination were not reduced during hydrogen reduction. They were supposed to suppress the aggregation of fine Ni particles during the MSR reaction. In contrast, oxides of Ni, Fe, and Sn formed during calcination were reduced to metallic Ni, Fe, and Sn, resulting the formation of Ni_3Fe, Ni_3Sn, and Ni_3Sn_2 intermetallic compounds that underwent significant aggregation during the hydrogen reduction treatment in the Ni–Fe and Ni–Sn coatings (Fig. 7). This caused a decrease in the BET specific surface area and activity. A similar aggregation of Ni particles occurred during the hydrogen reduction treatment of the Ni–0 coating, as shown in Fig. 7. Because Ni–0, Ni–Fe, and Ni–Sn showed similar BET specific surface areas, the activities of Ni–Fe and Ni–Sn were even lower than that of Ni–0, suggesting that the formation of Ni_3Fe and Ni_3Sn (Ni_3Sn_2) did not play a role in enhancing the MSR activity of the Ni honeycomb catalyst.

The differences in the Ni–Mg, Ni–Zr, Ni–Fe, and Ni–Sn microstructures after hydrogen reduction can be understood by considering the Gibbs free energy of the oxide formation

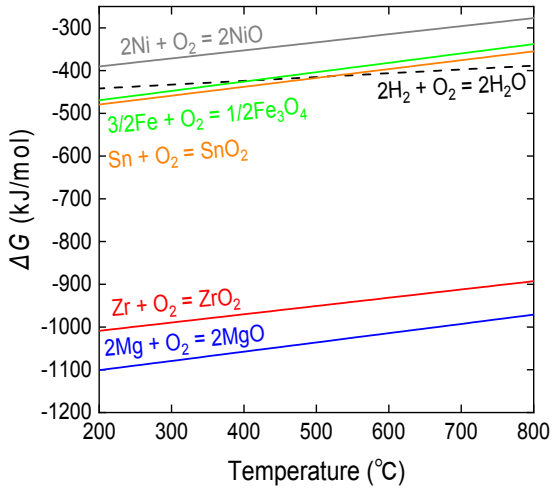

Fig. 10 An Ellingham diagram that shows the Gibbs free energy (ΔG) of the MgO, ZrO_2, Fe_3O_4, SnO_2, NiO, and H_2O formation as a function of the temperature.

(ΔG). Figure 10 shows an Ellingham diagram, which shows the ΔG of MgO, ZrO_2, Fe_3O_4, SnO_2, NiO, and H_2O as a function of temperature. It is clear that the ΔG of the formation of MgO and ZrO_2 is much lower than that of the formation of Fe_3O_4, SnO_2, NiO, suggesting that MgO and ZrO_2 can be formed easily. By comparing the ΔG values of hydrogen and other elements, it is possible to predict whether the oxide of the elements can be reduced by hydrogen, that is, if the absolute value of ΔG is smaller than that of the line indicated by hydrogen, the oxide can be reduced by hydrogen, and if the absolute value is larger, the oxide cannot be reduced by hydrogen. Thus, the Ellingham diagram indicates clearly that NiO, Fe_3O_4, and SnO_2 can be reduced by hydrogen at 430°C, which was the hydrogen reduction temperature used in this study, whereas MgO and ZrO_2 cannot. The Ellingham diagram provides guidelines for selecting a second element to form an active Ni/oxide coating on metallic honeycomb catalysts.

4. Conclusion

A bimetallic coating of Ni–Mg, Ni–Zr, Ni–Fe, and Ni–Sn on a high-cell-density Ni honeycomb catalyst was prepared by sequential impregnation, followed by calcination and reduction. Their catalytic performance for MSR was examined in the temperature range of 400–700°C. The catalytic performance was significantly improved by the coatings of Ni–Mg and Ni–Zr, whereas it was diminished by the coatings of Ni–Fe and Ni–Sn compared to that of the sample coated with only Ni. The enhanced catalytic performance of the Ni–Mg and Ni–Zr coatings was attributed to the formation of oxide-supported fine Ni particles, that is, $Ni/NiMgO_2$ and Ni/ZrO_2, which suppressed the aggregation of fine Ni particles during the reaction and lead to an improved catalytic performance. In contrast, no such oxide-supported fine Ni particles, but aggregated intermetallic compounds, Ni_3Fe and Ni_3Sn (Ni_3Sn_2), were formed in the Ni–Fe and Ni–Sn coatings after hydrogen reduction, resulting in a low catalytic activity.

Acknowledgments

The authors are grateful to Ms. Isaka and Ms. Nishimiya at the Electron Microscopy Analysis Station of NIMS for their help in preparing the cross-sectional samples using FIB equipment and TEM analysis. This work was supported by the Japan Society for the Promotion of Science through Grants-in-Aid for Scientific Research (Grants Nos. JP19H05817, JP19H05818, JP22H01804) and JST, CREST Grant No. JPMJCR2203, Japan.

REFERENCES

1) J.R. Rostrup-Nielsen: Phys. Chem. Chem. Phys. **3** (2001) 283–288.
2) J.D. Holladay, J. Hu, D.L. King and Y. Wang: Catal. Today **139** (2009) 244–260.
3) M. Torimoto and Y. Sekine: Catal. Sci. Technol. **12** (2022) 3387–3411.
4) J.A.M.A. Cybulski: *Structured Catalysts and Reactions*, ed. by J.A.M.A. Cybulski, (CRC Press, Boca Raton, FL, USA, 2005) pp. 1–17.
5) G. Groppi and E. Tronconi: Chem. Eng. Sci. **55** (2000) 2161–2171.
6) G. Groppi and E. Tronconi: Catal. Today **69** (2001) 63–73.
7) E. Tronconi and G. Groppi: Chem. Eng. Technol. **25** (2002) 743–750.
8) A. Cybulski and J.A. Moulijn: Chem. Eng. Sci. **49** (1994) 19–27.
9) R.J. Farrauto, Y. Liu, W. Ruettinger, O. Ilinich, L. Shore and T. Giroux: Catal. Rev. **49** (2007) 141–196.
10) C. Fukuhara, Y. Makiyama, K. Yamamoto and R. Watanabe: Chem. Lett. **42** (2013) 416–418.
11) C. Fukuhara, K. Yamamoto, Y. Makiyama, W. Kawasaki and R. Watanabe: Appl. Catal. A Gen. **492** (2015) 190–200.
12) Y. Hiramitsu, M. Demura, Y. Xu, M. Yoshida and T. Hirano: Appl. Catal. A Gen. **507** (2015) 162–168.
13) Y. Xu, T. Harimoto, T. Hirano, H. Ohata, H. Kunieda, Y. Hara and Y. Miyata: Int. J. Hydrogen Energ. **43** (2018) 15975–15984.
14) Y. Xu, T. Harimoto, L.S. Wang, T. Hirano, H. Kunieda, Y. Hara and Y. Miyata: Chem. Eng. Process. **129** (2018) 63–70.
15) Y. Xu, T. Hirano, H. Kunieda, Y. Hara and Y. Miyata: Catal. Sci. Technol. **10** (2020) 2004–2019.
16) T. Komatsu and S. Furukawa: Mater. Trans. **56** (2015) 460–467.
17) S. Furukawa and T. Komatsu: ACS Catal. **7** (2017) 735–765.
18) D.H. Chun, Y. Xu, M. Demura, K. Kishida, D.M. Wee and T. Hirano: J. Catal. **243** (2006) 99–107.
19) Y. Kaneno, T. Kondo, Y. Fujimoto, H. Tsuda, Y. Xu, M. Demura, H. Iwai, T. Hirano and T. Takasugi: Mater. Trans. **51** (2010) 1002–1010.
20) H. Mitani, Y. Xu, T. Hirano, M. Demura and R. Tamura: Catal. Today **281** (2017) 669–676.
21) Y. Xu, H.X. Jin, T. Hirano, Y. Matsushita and J.X. Zhang: Sci. Technol. Adv. Mater. **20** (2019) 622–631.
22) Y. Xu, J.Y. Yang, M. Demura, T. Hirano, Y. Matsushita, M. Tanaka and Y. Katsuya: Int. J. Hydrogen Energ. **39** (2014) 13156–13163.
23) M. D'Arino, F. Pinna and G. Strukul: Appl. Catal. B **53** (2004) 161–168.
24) R.G. Pavelko, A.A. Vasiliew, E. Llobet, X. Vilanova, N. Barrabes, F. Medina and V.G. Sevastyanov: Sens. Actuators B Chem. **137** (2009) 637–643.